IEEE Access
Multidisciplinary | Rapid Review | Open Access Journal

Date of publication xxxx 00, 0000, date of current version xxxx 00, 0000.

Digital Object Identifier

Ultrasound-based Visual Servoing for out-of-plane Longitudinal Needle Tracking in Robot-aided Percutaneous Nephrolithotomy

HOORIEH MAZDARANI[1], BEN SAINSBURY[2], JAMES WATTERSON[3], REBECCA HIBBERT[4], and CARLOS ROSSA[1]

[1]Dep. of Systems and Computer Engineering, Carleton University, Ottawa, ON Canada. (e-mail: hooriehmazdarani@cmail.carleton.ca; rossa@sce.carleton.ca)
[2]Marion Surgical, Seguin, ON, Canada (e-mail: ben@marionsurgical.com)
[3]Faculty of Medicine, Division of Urology, University of Ottawa, Ottawa, ON Canada (e-mail: jwatterson@toh.ca)
[4]Department of Radiology, Mayo Clinic, Rochester, MN USA (e-mail: hibbert.rebecca@mayo.edu)

This work was supported by the Natural Sciences and Engineering Research Council of Canada (NSERC), [funding ALLRP 580714-22]. Cette recherche a été financée par le Conseil de recherches en sciences naturelles et en génie du Canada (CRSNG), [no. de référ. ALLRP 580714-22].

ABSTRACT Percutaneous nephrolithotomy (PCNL) is a minimally invasive procedure to remove large renal calculi through a small incision in the patient's back. Ultrasound (US) imaging is commonly used to guide the needle to the kidney during this procedure. However, it requires an advanced level of dexterity to coordinate the US probe and the needle to keep the needle visible in the images at all times. Failure to maintain needle-probe alignment can result in inadvertent injury, bleeding, and other complications. The use of robotic assistance can alleviate the surgeon's cognitive workload by enabling autonomous positioning of the US probe and accurate needle tracking.

This paper presents a new US-guided visual servoing (VS) algorithm for needle tracking using longitudinal US images of a needle subjected to out-of-plane motion. The ultrasound probe can move in 4 degrees-of-freedom (DOF), that is, two translations and one rotation in the imaging plane, and one rotation out of the imaging plane. Unlike previously reported VS algorithms, 4-DOF tracking is achieved using only 2D-US images and without any additional position sensor or prior knowledge of the needle trajectory. The algorithm is validated extensively in three different experimental scenarios using a water tank, a tissue phantom, and ex-vivo porcine tissue. Results obtained from several trials confirm the algorithm's ability to track the needle and maintain needle-probe alignment with an average error of 1.5 mm, despite an out-of-plane average needle deflection of 7 mm along a 60 mm insertion depth.

INDEX TERMS Medical robotics, needle tracking, percutaneous nephrolithotomy, robot-assisted surgery, tool tracking, ultrasound imaging, visual servoing.

I. INTRODUCTION

PERCUTANEOUS nephrolithotomy (PCNL) is the primary surgical treatment to remove large upper urinary tract stones. In PCNL, the surgeon makes a small incision in the patient's back and inserts a small calibre tube to access the kidney. An endoscope is then passed down the tube into the kidney to fragment and remove the stones. Despite nearly half a century of continuous improvement, PCNL still has a steep learning curve and a high risk of complications such as bleeding, renal pelvis perforation, and colon and spleen injuries [1].

Kidney access during PCNL may be performed under fluoroscopy imaging, ultrasound (US) imaging, or a combination of both [2]. Fluoroscopy has been the main imaging modality used in Canada and in the United States; however, it exposes patients and interventionists to high levels of radiation [3], [4]. Moreover, other limitations of fluoroscopy include single-plane imaging, and the inability to image organs adjacent to the kidney during puncture, posing a risk of accidental injury [5]. In contrast, US-guided PCNL (usPCNL) is radiation-free and gives a clearer delineation of the kidney's adjacent structures, which can prevent inadvertent puncture [6], [7].

UsPCNL requires an advanced skill level to identify the

needle in the US images while steering it toward a target in the kidney. While inserting the needle with one hand, with the other hand the surgeon must orient the US probe either perpendicularly or parallel to the needle shaft in order to see it [8]. When the needle shaft crosses the imaging plane at a near-oblique angle, a cross-section of the needle shaft appears as a hyperechoic white dot in the image. This is called transverse imaging. To locate the needle tip, the surgeon slides the probe back and forth along the needle shaft. In the second case, where the imaging plane is parallel to the needle shaft, called longitudinal imaging, the needle appears as a line in the image. Although the needle tip is visible, manoeuvring the US probe to keep the same portion of the shaft visible in the image is not trivial [9]. Furthermore, when using bevelled-tip needles, the needle tip follows a curved trajectory during insertion, posing an additional challenge to keep the needle in the imaging plane [10], [11]. As a result, misinterpretation caused by image-needle misalignment is common, often leading to inaccurate needle placement and a steep learning curve [8], [12].

To assist surgeons in performing percutaneous image-guided needle puncturing and steering, a wide range of methods have been suggested, including a guide attached to the US probe to keep the needle aligned with the US plane [13], [14] at the cost of limited dexterity. Augmented reality has also been proposed [15]–[19]. More recently, robotic-assisted methods have been considered for other percutaneous procedures, such as prostate brachytherapy, thermal ablation of liver tumours, and kidney ablation [20]–[26]. In most of these methods, a robot arm steers the needle autonomously, while the position of the needle tip is measured through sensors embedded in the shaft, such as optical fibre or electromagnetic sensors [27]–[29]. When US images are used to track the needle, the imaging plane must move along with the needle to keep it visible at all times. For example, optical flow is used in [30] to segment a cannula from 2-dimensional (2D) US images and translate the probe to keep the needle centred in the image. In [31]–[33], the US probe is controlled to move along the pre-defined path the needle is expected to take.

Most of the methods described above rely on a pre-defined needle trajectory. However, in usPCNL the trajectory is not known as the needle is steered manually. To control the robot arm holding the US probe using only real-time US images, visual servoing (VS) may be used. In VS, visual features are defined to quantify the content of an image. The speed of the imaging sensor is then controlled to minimize the error between the real-time and the desired image features. The relation between the time derivatives of features and the speed of the imaging device is given by an interaction matrix, which contains the partial derivatives of the image features with respect to the speed of each degree-of-freedom (DOF) of the imaging sensor. A key consideration in VS is the choice of visual features. Image moments have been introduced as useful features for camera-based VS in [34], [35], and Green's theorem was used to find an analytical solution to the interaction matrix. Mebarki *et al.* followed with the first application of VS with image-moments derived from 2D US images in [36], and further in [37], where an analytical derivation of the interaction matrix with online parameter estimation was proposed to control the 6-DOFs of a US probe to image a cross-section of a motionless object with good convergence of the visual feature error. Further to that, [38] presented a new set of image features taken from three orthogonal US images, which provides global controller convergence even when considering symmetric objects. VS has also been used to position a needle in the US image plane during percutaneous cholecystectomy in [39], to adjust the in-plane rotation for image quality optimization in [40], and to scan peripheral arteries in [41]. In these examples, the US probe is manoeuvred to keep track of a static target. In usPCNL, the needle moves relative to the probe in an unpredictable manner.

In our previous work, we showed that image moment-based VS can effectively track a needle translating and rotating on a 2D plane [42]. This 2D tracking algorithm has a major practical limitation: If a bevelled needle is used, the needle tip follows a curved trajectory during insertion. Eventually, through this gradual out-of-plane motion, the needle shaft exits the imaging plane [43] until the algorithm is no longer able to track the needle. Attempts to mitigate this problem often model needle-tissue interaction to estimate needle deflection [11], [44]–[47]. Alternatively, volumetric US images provide more detailed information about the position of the needle and surrounding structures [38], [48]–[51]. However, 3D/4D US is not widely used in PCNL, and image processing is computationally expensive, resulting in lower frame rates than 2D imaging, which is not suitable for real-time control [52], [53]. Other methods use electromagnetic tracking, magnetic sensors, optical tracking systems, or other types of sensors attached to the needle to track the needle at the cost of additional equipment and added complexity [54]–[61].

In this paper, we extend the general concept of US-based VS from [37] and propose a new set of moment-based image features specifically devised for needle tracking with out-of-plane motion caused by needle deflection, using only 2D-US images. While image moments and VS have previously been used for US-guided tool tracking, to the best of the author's knowledge, this is the first time that image moments derived from single-plane 2D US images are used with VS for tracking a needle subjected to out-of-plane deflection. Here, needle motion is considered in 4-DOFs, that is, two translations and one rotation of the needle in the US imaging plane, and one rotation out of the imaging plane. In contrast to the algorithms described earlier, needle tracking is done in 4-DOF without any prior knowledge of the needle trajectory and solely based on 2D US images. The main contributions of this work are:

1) This is the first VS method with image moments derived specifically for tracking both in-plane and out-of-plane motion of a moving needle using longitudinal US images; and
2) The algorithm only requires a standard 2D US probe

and does not rely on any prior knowledge of the needle trajectory.

Running at 20 Hz, the method is computationally efficient and well-suited for real-time needle tracking. In the proposed approach, the US probe is attached to a robotic manipulator to follow the motion of a manually steered needle in the tissue. A desired longitudinal pose of the needle in the US image is first defined, followed by a set of image features calculated from the desired and real-time images, from which the interaction matrix is calculated for the image. As the needle is advanced in the tissue, the algorithm determines the required linear and angular velocities of the US probe that minimize the difference between the desired and real-time image features, ensuring that the needle shaft is always aligned with the US imaging plane.

The paper is organized as follows: Section 2 introduces the proposed VS algorithm, the image features, and the robot control law. The experimental procedure is presented in Section 3. In the experimental setup, the US probe is connected to a force sensor-equipped robot arm, and a second robot is used to move the needle with measurable and repeatable movements. Three experimental scenarios are considered. First, the needle and probe are submerged in a water container so that both the needle and probe can be moved freely. Then, a phantom made of 5% agar is employed to validate the algorithm's ability of tracking the needle as it deflects in the tissue. Finally, the algorithm's functionality is tested in *ex-vivo* porcine tissue for more realistic results. The feasibility of the proposed method is demonstrated through several trials in Section 4. Finally, in Section 5, a discussion of the obtained results and recommendations for future work are presented.

II. 4-DOF VISUAL SERVOING DESIGN

The first step in the algorithm is to define a desired longitudinal US image of the needle and a set of predefined time-variant and differentiable visual features that quantify the content of the image. The robot is then controlled so that the visual features extracted from the real-time US image converge to their corresponding values in the desired US image [34].

Fig. 1(a) shows a sample of a longitudinal US image of a needle placed in a water tank, where the plane containing the needle shaft is aligned with the US imaging plane, making the needle appear as a bright line in the image. The features describing the characteristics of the image are the visible length ℓ of the needle, the position of the needle tip in the image (x_{tip}, y_{tip}), and the in-plane orientation θ of the needle shaft measured with respect to the image horizontal axis x. When a bevelled tip needle is employed, the tip follows a curved trajectory. As a result, when the needle moves away from a straight-line trajectory, the longitudinal plane containing the needle shaft slowly rotates with respect to the US imaging plane. This out-of-plane motion lowers the intensity of the pixels along the needle shaft, particularly around the tip, and gradually decreases the needle's visible length ℓ, see Fig. 1(b). The decrease in image intensity can be clearly

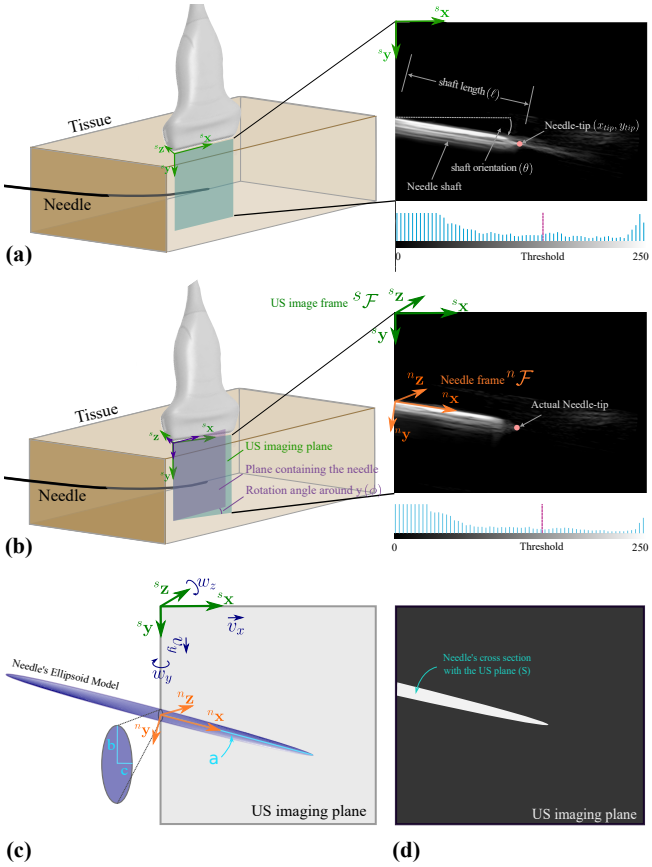

FIGURE 1. Longitudinal US image of a needle in a water tank. In (a), the plane containing the needle shaft is aligned with the US imaging plane (x, y). In (b), these planes are rotated 8° about y. We can distinguish 4 independent features in the image: 1) the needle's shaft length ℓ, 2) the position of the needle tip (x_{tip}, y_{tip}), 3) the in-plane orientation of the shaft θ, and 4) the out-of-plane misalignment ϕ between the needle and the imaging planes about y. The out-of-plane misalignment decreases the image intensity from (a) to (b) and the length ℓ. In (c) the needle is modelled as a semi-ellipsoid in the given coordinate frames. In (d), the needle's cross-section is shown as S.

seen by comparing each US image and histograms presented under them in Fig. 1(a) and (b). Thus, concurrent variations in both image intensity and needle length indicate out-of-plane rotation, which is quantified by the variable ϕ as defined in Fig. 1(b).

Assuming a needle inserted in soft tissue, the following simplifications can be made:

1) The visible portion of the needle in the US image is a straight line;
2) The needle can only translate along the x and y axes, and rotate about the y and z axes in the US coordinate frame, as defined in Fig. 1(a);
3) The orientation of the needle tip bevel is known, thus the direction of potential out-of-plane motion about the y axis, that is $\text{sign}(d\phi/dt)$, is also known.

Hereafter, we give vectors and matrices lower and upper case variables, respectively, written in bold typeface. Since our goal is to track the needle's motion in 4-DOF (translations along the x and y axes and rotations about the y and z axes),

let $\mathbf{v} \in \mathcal{R}^{4\times 1}$ be the velocity of the US probe defined as

$$\mathbf{v} = [\boldsymbol{\upsilon} \quad \boldsymbol{\omega}]^T = [\upsilon_x \quad \upsilon_y \quad \omega_y \quad \omega_z]^T \tag{1}$$

where $\boldsymbol{\upsilon} = [\upsilon_x \quad \upsilon_y]^T$ has the translational velocity of the probe along x and y, that is v_x and v_y respectively, and $\boldsymbol{\omega} = [\omega_y \quad \omega_z]^T$ represents the rotational components of probe velocity about the y and z axes, that is ω_y and ω_z, respectively. The US probe position is measured in ${}^s\mathcal{F}$, as specified in Fig. 1(b). The needle pose is given by the four independent features x_{tip}, y_{tip}, θ, and ϕ, which are used to track the in-plane and out-of-plane motion of the needle. The vector of image features can be defined as:

$$\mathbf{s} = [x_{tip} \quad y_{tip} \quad \theta \quad \phi]^T \tag{2}$$

These features are decoupled since x_{tip}, y_{tip}, and θ are indicators of in-plane motion, whereas ϕ indicates the out-of-plane motion. The variation of image features with respect to probe velocities can then be written as:

$$\dot{s}_i = \frac{\partial s_i}{\partial v_x} v_x + \frac{\partial s_i}{\partial v_y} v_y + \frac{\partial s_i}{\partial \omega_y} \omega_y + \frac{\partial s_i}{\partial \omega_z} \omega_z, \tag{3}$$

where the dot operator represents the first temporal derivative, and the subscript i indicates the i^{th} element of vector $\mathbf{s}$. We now relate the visual features' time variation $\dot{\mathbf{s}}$ to the probe's velocity through the so called interaction matrix $\mathbf{L}_s$:

$$\dot{\mathbf{s}} = \mathbf{L}_s \mathbf{v} \tag{4}$$

where the i^{th} row of the interaction matrix has all the partial derivatives of the i^{th} feature with respect to the probe velocities, that is:

$$\mathbf{L}_{s_i} = \left[\frac{\partial \mathbf{s}_i}{\partial v_x} \quad \frac{\partial \mathbf{s}_i}{\partial v_y} \quad \frac{\partial \mathbf{s}_i}{\partial \omega_y} \quad \frac{\partial \mathbf{s}_i}{\partial \omega_z} \right]. \tag{5}$$

Since the velocity vector has 4 elements and a vector of 4 features is considered, $\mathbf{L}_s \in \mathcal{R}^{4\times 4}$. Further, since all 4 image features are decoupled from one another, as stated earlier, $\mathbf{L}_s$ will be full-rank and the velocity of the US probe can be calculated through (4). Stable VS control based on 2D US images then requires the following 3 additional conditions to be met [37]:

4) A distinguishable cross-section of the needle is visible in the US image;
5) All points in the needle's surface can be captured by a function $f_n(x, y, z) = 0$;
6) $\boldsymbol{\nabla} f_n(x, y, z)$ exists.

Considering that tracking starts when a cross-section of the needle becomes visible in the US image, a functional tracking system will ensure that the first condition is fulfilled. To satisfy the second and third conditions, the needle can be modelled as a prolate spheroid, as depicted in Figs. 1(c) and (d). The general ellipsoid, also known as the triaxial ellipsoid, can be defined in Cartesian coordinates as:

$$\frac{x^2}{a^2} + \frac{y^2}{b^2} + \frac{z^2}{c^2} = 1, \tag{6}$$

where a, b, and c are the lengths of the principal semi-axes. When $a \neq b = c$, the ellipsoid is a spheroid, and in particular, if $a > b = c$ it becomes a prolate spheroid. Equation (6) can be written in the form of $f_n(x, y, z) = 0$ as:

$$f_n(x, y, z) = \frac{x^2}{a^2} + \frac{y^2}{b^2} + \frac{z^2}{c^2} - 1. \tag{7}$$

The next step is to calculate the visual features from each US image. Such image features can be defined in terms of image moments of different orders, which are statistical descriptors of objects in the image plane [35]. The rest of this section details how the image features and their derivatives are defined using image moments. Finally, the interaction matrix derived from these features is employed to design the VS controller.

A. DEFINITION OF IMAGE MOMENTS

Image moments of order $i + j$ may be defined as:

$$m_{ij} = \iint_{\mathcal{S}(t)} f(x, y, t) dx dy; \quad f(x, y, t) = x^i y^j I(x, y, t) \tag{8}$$

where (x, y) are coordinates of a point in the image, $I(x, y, t)$ is the intensity value of each point at time t, and $\mathcal{S}(t)$ is the area in the image containing the cross-section image of the needle in the image, see Fig. 1(c). Now, image features in (2) can be defined as functions of image moments as:

$$s_k = g_k(m_{i,j}); \quad k = 1, \ldots, 4 \text{ and } \forall i, j \geq 0 \tag{9}$$

where s_k is the k^{th} feature in vector $\mathbf{s}$, whose time derivative becomes:

$$\dot{s}_k = \frac{\partial g_k}{\partial m_{ij}} \dot{m}_{ij}; \quad k = 1, \ldots, 4 \text{ and } \forall i, j \geq 0 \tag{10}$$

To calculate $\dot{m}_{ij}$, we can apply Leibniz integral rule to (8), which yields [34]:

$$\dot{m}_{ij} = \iint_{\mathcal{S}(t)} \left(\frac{\partial f}{\partial t} + \text{div} \left[f(x, y) [\dot{x} \quad \dot{y}]^T \right] \right) dx dy \tag{11}$$

where $\dot{x}$ and $\dot{y}$ are the image point velocities between consecutive images. Expanding (11) gives:

$$\dot{m}_{ij} = \iint_{\mathcal{S}(t)} \left[x^i y^j \dot{I} + \frac{\partial f}{\partial x} \dot{x} + \frac{\partial f}{\partial y} \dot{y} + f(x, y) \left(\frac{\partial \dot{x}}{\partial x} + \frac{\partial \dot{y}}{\partial y} \right) \right] dx dy \tag{12}$$

Here, $\dot{I}$, short for $\dot{I}(x, y, t)$, is the variation in the intensity of each pixel in consecutive images. The next step is to calculate $\dot{x}$ and $\dot{y}$ based on the needle image model defined in the previous subsection. The approach taken here is similar to the one introduced in [37] with modifications for out-of-plane motion compensation. However, the complete methodology is provided for clarity and comprehensiveness. Refereeing now to Fig. 1(d), for any point ${}^n\mathbf{p} = [{}^n x \ {}^n y \ {}^n z]^T$ in the needle's frame ${}^n\mathcal{F}$, the following affine transformation gives the point's coordinates in the US probe's frame:

$${}^s\mathbf{p} = {}^s\mathbf{R}_n \, {}^n\mathbf{p} + {}^s\mathbf{t}_n \tag{13}$$

where ${}^s\mathbf{R}_n$ and ${}^s\mathbf{t}_n = [t_x \ t_y \ t_z]^T$ are the rotation matrix and the translation vector, relating two coordinate frames ${}^s\mathcal{F}$ and ${}^n\mathcal{F}$,

and ${}^s\mathbf{p} = [x\ y\ 0]^T$ is the coordinate of a point in the US image for $z = 0$ defined in the US coordinate frame ${}^s\mathcal{F}$. The rotation matrix is:

$$\begin{aligned} {}^s\mathbf{R}_n &= \mathbf{R}_\mathbf{z}(-\theta)\mathbf{R}_\mathbf{y}(-\phi) \\ &= \begin{bmatrix} \cos\theta\cos\phi & \sin\theta & -\cos\theta\sin\phi \\ -\sin\theta\cos\phi & \cos\theta & \sin\theta\sin\phi \\ \sin\phi & 0 & \cos\phi \end{bmatrix} \end{aligned} \tag{14}$$

where θ is the azimuthal angle between the needle shaft and the x-axis in the $x-y$ plane, and ϕ is the elevation angle between the needle shaft and the $x-y$ plane, both defined in the US probe coordinate frame. Assuming that the needle's coordinate frame is located along the US probe's y-axis, the translation vector has only one non-zero element, that is:

$${}^s\mathbf{t}_n = \begin{bmatrix} 0 & t_y & 0 \end{bmatrix}^T \tag{15}$$

To calculate $\dot{x}$ and $\dot{y}$ the time derivative of (13) is taken:

$${}^s\dot{\mathbf{p}} = {}^s\dot{\mathbf{R}}_n\,{}^n\mathbf{p} + {}^s\mathbf{R}_n\,{}^n\dot{\mathbf{p}} + {}^s\dot{\mathbf{t}}_n \tag{16}$$

in which:

$$\begin{cases} {}^s\dot{\mathbf{R}}_n = -[\boldsymbol{\omega}]_\times\,{}^s\mathbf{R}_n \\ {}^s\dot{\mathbf{t}}_n = -[\boldsymbol{\omega}]_\times\,{}^s\mathbf{t}_n - \boldsymbol{v} \end{cases} \tag{17}$$

Here, $[\boldsymbol{\omega}]_\times$ represents the cross product matrix (or the skew-symmetric matrix) associated with vector $\boldsymbol{\omega}$. It follows that:

$${}^s\dot{\mathbf{p}} = -[\boldsymbol{\omega}]_\times\,{}^s\mathbf{R}_n\,{}^n\mathbf{p} - \boldsymbol{v} - [\boldsymbol{\omega}]_\times\,{}^s\mathbf{t}_n + {}^s\mathbf{R}_n\,{}^n\dot{\mathbf{p}}, \tag{18}$$

and from (13), the above simplifies to:

$${}^s\dot{\mathbf{p}} = -\boldsymbol{v} - [\boldsymbol{\omega}]_\times\,{}^s\mathbf{p} + {}^s\mathbf{R}_n\,{}^n\dot{\mathbf{p}} \tag{19}$$

For skew-symmetric matrices, $[\boldsymbol{a}]_\times\boldsymbol{b} = -[\boldsymbol{b}]_\times\boldsymbol{a}$, thus (19) can be rewritten as:

$${}^s\dot{\mathbf{p}} = -\boldsymbol{v} + [{}^s\mathbf{p}]_\times\boldsymbol{\omega} + {}^s\mathbf{R}_n\,{}^n\dot{\mathbf{p}}. \tag{20}$$

Here, it is desirable to express ${}^s\dot{\mathbf{p}} = [\dot{x}\ \dot{y}\ 0]$ only in terms of ${}^s\mathbf{p}$, $\boldsymbol{v}$ and $\boldsymbol{\omega}$. To eliminate ${}^n\dot{\mathbf{p}}$, the method provided in [37] can be employed herein.

Unless the needle has pure in-plane motion, a different cross-section of the needle is visible in the US image at each sampling time. The velocity of a contour point ${}^n\mathbf{p}(k) \in \mathcal{C}(k)$ in image k can be approximated as ${}^n\mathbf{p}(k) - {}^n\mathbf{p}(k-1)$. For in-plane motion, since the contour $\mathcal{C}$ remains the same for different samples, ${}^n\dot{\mathbf{p}} \approx 0$. Therefore, ${}^n\dot{\mathbf{p}} \neq 0$ indicates the out-of-plane motion occurred between two image samples. Any point ${}^n\mathbf{p} \in \mathcal{C}$ results from the intersection of the US plane with the needle surface f_n. Therefore, vector ${}^n\dot{\mathbf{p}}$ lies on the plane tangent to the needle surface at ${}^\mathbf{n}\mathbf{p}$. The following relationship can be used:

$$({}^n\boldsymbol{\nabla} f_n)^T\,{}^n\dot{\mathbf{p}} = 0 \tag{21}$$

where ${}^n\boldsymbol{\nabla} f_n$ is the gradient of f_n in the needle frame. The projection of $\mathbf{z}_s$-axis on the plane tangent to the needle surface at ${}^n\mathbf{p}$ is the closest direction for ${}^n\dot{\mathbf{p}}$. Therefore, the second relationship for ${}^n\dot{\mathbf{p}}$ can be established as:

$$({}^n\mathbf{z}_s \times {}^n\boldsymbol{\nabla} f_n)^T\,{}^n\dot{\mathbf{p}} = 0 \tag{22}$$

By solving for (20)-(22), the image point velocity can be written as:

$$\begin{cases} \dot{x} = -v_x + xk_1\omega_y + y\omega_z \\ \dot{y} = -v_y + xk_2\omega_y - x\omega_z \end{cases} \tag{23}$$

in which k_1 and k_2 are:

$$k_1 = \frac{f_x f_z}{f_x^2+f_y^2}, \quad k_2 = \frac{f_y f_z}{f_x^2+f_y^2} \tag{24}$$

and ${}^s\boldsymbol{\nabla} f_n = [f_x\ f_y\ f_z]^T$ is the gradient of $f_n(x,y,z)$ in the US probe's frame, i.e., ${}^s\boldsymbol{\nabla} f_n = {}^s\mathbf{R}_n\,{}^n\boldsymbol{\nabla} f_n$, which can be derived by first calculating ${}^n\boldsymbol{\nabla} f_n$ based on (7) as:

$${}^n\boldsymbol{\nabla} f_n = \begin{bmatrix} \frac{2}{a^2}\,{}^n x & \frac{2}{b^2}\,{}^n y & \frac{2}{c^2}\,{}^n z \end{bmatrix}^T = \mathbf{A}\,{}^n\mathbf{p}, \tag{25}$$

where $\mathbf{A} = \operatorname{diag}\left(\frac{2}{a^2}, \frac{2}{b^2}, \frac{2}{c^2}\right)$ and ${}^n\mathbf{p} = {}^s\mathbf{R}_n^T({}^s\mathbf{p} - {}^s\mathbf{t}_n)$. Therefore, the gradient vector in the US frame is:

$${}^s\boldsymbol{\nabla} f_n = {}^s\mathbf{R}_n\,{}^n\boldsymbol{\nabla} f_n = {}^s\mathbf{R}_n A\,{}^s\mathbf{R}_n^T({}^s\mathbf{p} - {}^s\mathbf{t}_n). \tag{26}$$

By substituting ${}^s\mathbf{R}_n$ from (14) in (26), assuming $b = c$, and using the small angel approximations $\sin^2\phi \simeq 0$, and $\cos\phi \simeq 1$, ${}^s\boldsymbol{\nabla} f_n$ can be written as:

$${}^s\boldsymbol{\nabla} f_n = \frac{2}{a^2b^2}\begin{bmatrix} (a^2s^2\theta + b^2c^2\theta)x + (a^2-b^2)s\theta c\theta y' \\ (a^2-b^2)s\theta c\theta x + (a^2c^2\theta + b^2s^2\theta)y' \\ -(a^2-b^2)c\theta s\phi x + (a^2-b^2)s\theta s\phi y' \end{bmatrix} \tag{27}$$

with $\sin \to s$, $\cos \to c$, and $y' = y - t_y$. The model parameters from (6) needed in (27) are a and b, which are both measurable from the desired US image, where $a = \ell^*$ is the length of needle shaft in the desired image, and b is the needle diameter. While the needle diameter is usually known, it can also be calculated form the image. However, by considering that $a \gg b$, the gradient vector can be approximated as follows, which is more convenient for further calculations:

$${}^s\boldsymbol{\nabla} f_n \approx \begin{bmatrix} s^2\theta x + s\theta c\theta y' \\ s\theta c\theta x + c^2\theta y' \\ -c\theta s\phi x + s\theta s\phi y' \end{bmatrix} \tag{28}$$

Finally, by substituting (23) in (12), the time variation of image features can be written in terms of probe velocities as:

$$\dot{m}_{ij} = \begin{bmatrix} m_{ij_{vx}} & m_{ij_{vy}} & m_{ij_{\omega y}} & m_{ij_{\omega z}} \end{bmatrix}\mathbf{v} \tag{29}$$

where $m_{ij_{vx}} = \frac{\partial m_{ij}}{\partial v_x}$, $m_{ij_{vy}} = \frac{\partial m_{ij}}{\partial v_y}$, and so on.

B. VISUAL FEATURES CALCULATION

The visual features defined in Fig. 1(a) can now be written in terms of moments of order of up to two. The needle shaft orientation with respect to the horizontal imaging axis is:

$$\theta = \frac{1}{2}\arctan\left(\frac{2\mu_{11}}{\mu_{20}-\mu_{02}}\right), \tag{30}$$

and the length of the needle shaft in the image is:

$$\ell = \sqrt{\frac{8}{m_{00}}\left(\mu_{20}+\mu_{02}+\sqrt{(\mu_{20}-\mu_{02})^2+4\mu_{11}^2}\right)}, \tag{31}$$

and the position of the needle tip in the image is:

$$\begin{aligned} x_{tip} &= l\cos\theta \\ y_{tip} &= \frac{m_{01}}{m_{00}} + \frac{1}{2}l\sin\theta. \end{aligned} \tag{32}$$

The needle diameter required in (27) can be also defined as:

$$b = \sqrt{\frac{8}{m_{00}}\left(\mu_{20}+\mu_{02}-\sqrt{\left(\mu_{20}-\mu_{02}\right)^2+4\mu_{11}^2}\right)}, \tag{33}$$

which is only computed once from the desired image. Here, μ_{ij} is known as the central moment and is defined by:

$$\mu_{ij} = \iint_{\mathcal{S}} (x-x_g)^i (y-y_g)^j \, dxdy \tag{34}$$

where $x_g = \frac{m_{10}}{m_{00}}$ and $y_g = \frac{m_{01}}{m_{00}}$ give the coordinates of the centre of gravity. The relation between μ_{ij} and m_{ij} is given in [34] as:

$$\mu_{ij} = \sum_{k=0}^{i}\sum_{l=0}^{j} \binom{i}{k}\binom{j}{l} (-x_g)^{i-k} (-y_g)^{j-l} m_{kl} \tag{35}$$

Therefore, the central moments can be calculated as:

$$\begin{aligned} \mu_{11} &= m_{11} - x_g m_{01} = m_{11} - y_g m_{10} \\ \mu_{20} &= m_{20} - x_g m_{10} \\ \mu_{02} &= m_{02} - y_g m_{01} \end{aligned} \tag{36}$$

As postulated at the beginning of this section, the image intensity plays a key role in determining out-of-plane motion. Therefore, we can define an intensity-based feature as follows:

$$\alpha = m_{00} = \iint_{\mathcal{S}} I(x,y,t)dxdy. \tag{37}$$

This zero-order moment gives the object's area weighed by its pixels' intensity. While out-of-plane motion gradually decreases both the image intensity and needle length in the image, with in-plane motion these parameters will not change considerably, and thus they can be used to estimate the out-of-plane rotation of the needle.

By considering a spherical coordinate system for the ellipsoid model given in Fig. 1(c), the elevation angle ϕ can be defined as:

$$\phi = \arcsin\sqrt{\frac{a^2-r^2}{a^2-b^2}}, \tag{38}$$

where r is the distance of each point on the ellipsoid surface to the origin. To calculate ϕ, we note that $a \gg b$ and $b \leq r \leq a$. Also, a is equal to the needle length in the desired image while r is equal to the needle length in the current image, that is, $a = \ell^*$ and $r = \ell$. Further, (38) is only valid when both the visible needle length ℓ and needle's intensity (given by α) are less than the values defined in the desired image. Therefore, by considering these observations and using the small angel approximation $\sin\phi \approx \phi$ in (38), the out-of-plane rotation can be approximately calculated by:

$$\phi = cH(l^*-l)H(\alpha^*-\alpha)\sqrt{1-\left(\frac{l}{l^*}\right)^2}, \tag{39}$$

where $H(.)$ is the Heaviside step function, $0 < c < 1$ is a tunable weight, and ℓ^* and α^* are, respectively, the needle's length and intensity in the desired image. We also notice that in the defined coordinate system ϕ is invariant to in-plane motion.

Finally, by calculating the time variation of visual features in $\mathbf{s} = [x_{tip} \quad y_{tip} \quad \theta \quad \phi]^T$ according to (10), the interaction matrix $\mathbf{L}_s$ in (4) is known for every time step. The interaction matrix can now be used in the controller design to calculate the probe velocities.

C. ROBOT CONTROLLER DESIGN

A classic control law widely used in VS gives the velocity of the camera (here the US probe) based on the error observed between the desired features $\mathbf{s}^*$ and the actual time-variant image features $\mathbf{s}(t)$ calculated on the real-time US images. Defining the error signal as $\mathbf{e}(t) = \mathbf{s}^* - \mathbf{s}(t)$, the VS control law that minimizes the features' error is:

$$\mathbf{v_c} = \mathbf{K}_p \mathbf{L}_s^{\dagger} (\mathbf{s}^* - \mathbf{s}) \tag{40}$$

where $\mathbf{v_c}$ is the US probe's velocity, $\mathbf{K}_p > 0 \in R^{4\times4}$ is a diagonal matrix of control gains, and $\mathbf{L}_s^{\dagger}$ is the pseudo-inverse of $\mathbf{L}_s$ given by

$$\mathbf{L}_s^{\dagger} = \mathbf{L}_s^T \left(\mathbf{L}_s \mathbf{L}_s^T\right)^{-1} \tag{41}$$

With a correct estimation of $\mathbf{L}_s$, the closed-loop system is shown to be locally asymptotically stable [37]. Here, the desired feature vector $\mathbf{s}^*$ represents the desired cross-section image of the needle, which in turn defines the desired pose of the robot arm holding the US probe. The basic block diagram of the proposed tracking method is shown in Fig. 2, and control algorithm is briefly explained in Algorithm 1.

During imaging, the US probe must remain in contact with the tissue surface, which may be enforced with a force controller along the vertical axis. Thus, a force sensor is added to the robot end-effector and a similar force controller as the one implemented in [50] is applied. Such internal force control loop will determine the position of the probe along the y-axis in such a way to regulate the contact force to 2 N, and its angle around the z-axis to deal with uneven surfaces. Therefore, while the VS controller tries to track the needle with both in-plane and out-of-plane motions, the internal force controller keeps the probe in contact with the tissue.

III. EXPERIMENTAL VALIDATION

To validate the proposed method, the experimental setup shown in Fig. 3 is used. A 40-mm US probe (L15-7H40-A5 from Telemed Ultrasound, Vilnius, Lituania) is attached to the end-effector of a 6-DOF robot arm (Meca500 from Mecademic, Montréal, Canada) through a force sensor (Medusa FT sensor from Bota Systems, Zurich, Switzerland). Both convex and linear US transducers can be used for usPCNL. The former is preferred for deep organs and the latter for shallower areas [13]. In this paper, we used a linear transducer, however, the proposed algorithm can be implemented using a convex probe as well. The US machine streams images

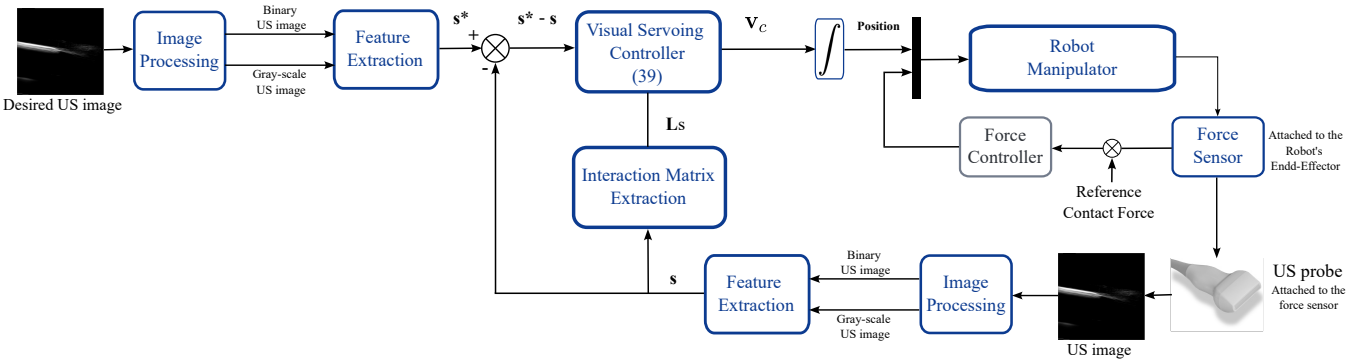

FIGURE 2. **Overview of the proposed algorithm. Image features extracted from a desired US image and the real-time US image are multiplied by a time-variant interaction matrix to determine the required speed of the US probe that makes the current features tend to the desired features. The force controller is used in Scenario 2 to ensure sufficient acoustic contact between the tissue and the US probe.**

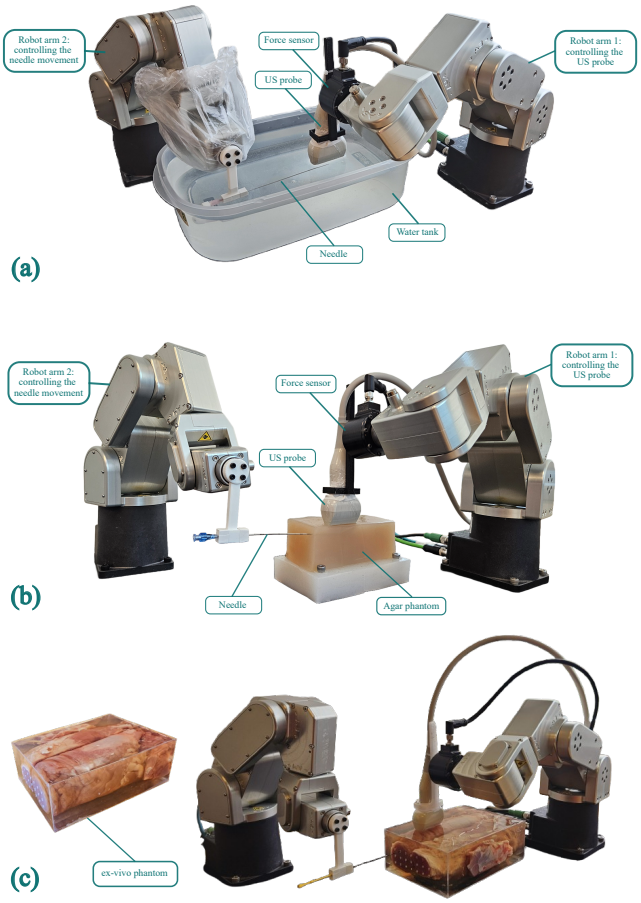

FIGURE 3. **Experimental setup. In (a), the needle and the US probe are each connected to a robot arm and submerged in a water tank. As robot 2 moves the needle in a random sequence in a plane, robot 1 adjusts the position and orientation of the US to minimize the error between the desired and actual image features. In (b), the water tank is replaced with an artificial phantom. In (c), ex-vivo porcine tissue is used in the experiments.**

Algorithm 1 US-based VS for longitudinal Needle Tracking

Initializing:
Capture desired US image
Extract image features (30), (32), and (39)
while needle is being inserted **do**
  Capture real-time US image
  Extract image features (30), (32), and (39)
  Update interaction matrix $\mathbf{L}_s$
  Calculate probe velocities $\mathbf{v_c}$ (40)
  if probe-tissue contact is required **then**
    Read force data
    Apply internal force controller
  end if
end while

TABLE 1. **Ultrasound image acquisition parameters**

frequency	gain	focus	depth	dyn. range	power
10 MHz	79 %	14-21 mm	40 mm	72 dB	−4 dB

in real-time at 50 Hz according to the specifications given in Table 1. A standard 18-gauge bevelled tip percutaneous access needle is attached to a second robot arm that controls the needle movement. While in practice needle insertion is performed manually, here we use a second robot arm to ensure repeatable and measurable experimental trials. On average, when inserted to a depth of 100-140 mm, an 18-G bevelled tip needle deflects by 6-12 mm from a straight line [11], [44], which is enough to test the proposed algorithm. The algorithm is implemented on an Intel(R) Core i7-9700K computer with a 3.60 GHz CPU, 128 GB of RAM, and a GeForce RTX 4060 graphics card. Matlab is used for both US image acquisition and robot control, with a sampling rate of 20 Hz. The robots communicate with the controller via EtherCAT and TwinCAT3.

Once the needle is positioned in the medium, the robot holding the US probe is moved manually until the needle becomes visible in the US image. Then the target image is captured and stored. Afterwards, while one robot is controlled

to move the needle, the second robot autonomously manoeuvres the US probe according to the velocities calculated by the VS controller. The proportional control gains are set to $\mathbf{K}_p = \text{diag}(0.5, 0.5, 0.2, 0.2)$. Binary threshold image segmentation is applied to real-time US images to generate binary images to be used along with the raw grey-scale image, both in the close vicinity of the tracked needle, in calculating the interaction matrix, as shown in Fig. 1b. Three experimental scenarios are considered using a water tank, an agar phantom, and *ex-vivo* porcine tissue.

Scenario 1: In the first set of experiments, the needle is submerged in a water tank to allow free movement in 4-DOF, see Fig. 3(a). The robot holding the needle moves it base along a random path with linear and angular velocities of $0 \leq \upsilon_x \leq 6$ mm/s, $0 \leq \upsilon_y \leq 2$ mm/s, $0 \leq \omega_y \leq 0.017$ rad/s, and $0 \leq \omega_z \leq 0.025$ rad/s - the latter induces out-of-plane rotation of the needle compared to the imaging plane. Although the needle does not bend in water, the robot exaggerates out-of-plane motion to fully demonstrate the algorithm's functionality.

Scenario 2: The needle is inserted in 5% agar phantom suitable for ultrasound imaging [62] with its bevelled tip approximately directed towards the positive z-axis (i.e., out of the imaging plane), see Fig. 3(b). The robot moves the needle's base along a straight line with a velocity of $\upsilon_x = 3$ mm/s. As the needle is pushed into the tissue, the bevelled tip causes the needle to deflect about its y-axis. To ensure that the US probe remains in contact with the tissue surface, a force control loop is used to regulate υ_y and ω_z.

Scenario 3: A fresh piece of porcine tenderloin muscle embedded in porcine gelatin is used, see Fig. 3(c). All other experimental conditions are the same as in Scenario 2.

In each Scenario, 10 trials were run for 20-25 seconds each. The features' error and the position of each robot arm are then evaluated. Each trial in Scenarios 2 and 3 uses a different needle insertion point in the tissue.

IV. RESULTS AND DISCUSSION

Fig. 4 (top) shows the measured 3D displacement of the needle and centre of image frame (${}^n\mathcal{F}$ and ${}^s\mathcal{F}$, respectively) in a representative trial in Scenario 1. The 3D displacement error between the US probe and the needle tip is shown in Fig. 4 (bottom) with an average of 1.56 mm. Fig. 5 shows the observed features error for 10 trials of this scenario, with an average error of less than 1.6 mm in needle tip position and less than 1° error in the shaft orientation.

In Scenario 2, the robot only pushes the needle into the tissue along its x-axis. The bevel of the needle is directed toward the z-axis, which results in out-of-plane deflection. To measure the amount of needle deflection, at the end of the tracking, the robot holding the probe rotates it 90° so that a transverse cross section of the needle is visible in the US image. The robot then scans the needle shaft as it moves the probe from the needle tip back to its insertion point. The coordinates of the centre of the needle's cross section are then labelled manually in the transverse images.

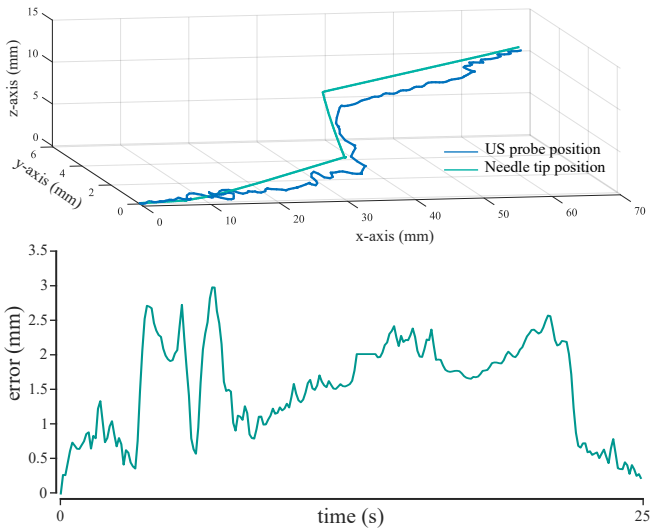

FIGURE 4. **Measured displacement of the US probe and needle tip in a trial from Scenario 1 (top) and the 3D displacement error between the needle's tip and US probe (bottom).**

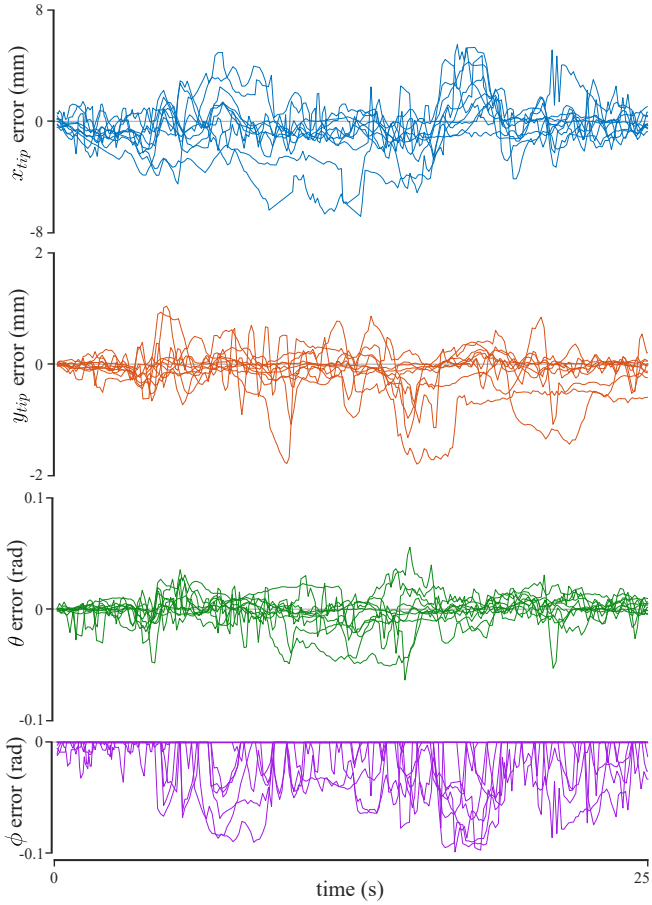

FIGURE 5. **Calculated error between desired and actual image features for x_{tip}, y_{tip}, θ, and ϕ for all 10 trials in Scenario 1.**

TABLE 2. Mean and standard deviation of feature errors ($s^* - s$) over 10 trials in each scenario

	$e_{x_{tip}}$ (mm)		$e_{y_{tip}}$ (mm)		e_θ (rad)		e_Φ (rad)	
Test scenario	mean	sd	mean	sd	mean	sd	mean	sd
Scenario 1	-1.58	1.12	-0.21	0.19	0.009	0.01	-0.013	0.02
Scenario 2	-1.238	0.88	-1.09	1.33	-0.023	0.04	-0.005	0.01
Scenario 3	-1.46	1.06	0.52	0.31	0.005	0.03	-0.018	0.01

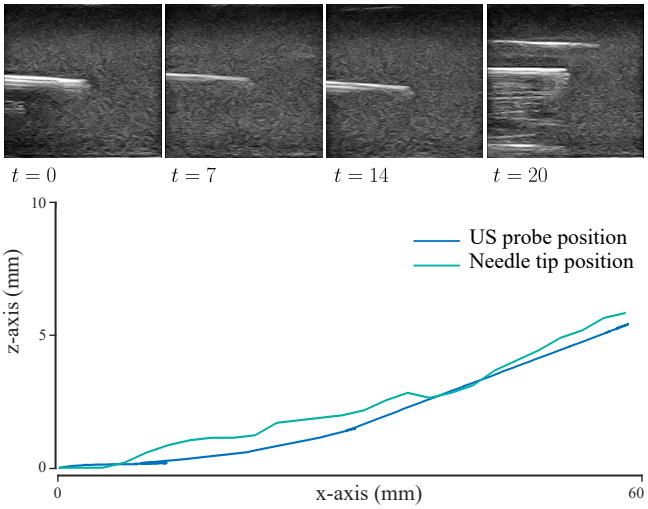

FIGURE 6. Measured displacement of the US probe and the needle's tip in Scenario 2 on the $x - z$ plane along with four US images of the needle. The needle's position is measured in each transverse image along the needle shaft.

Fig. 6 shows the displacement of the needle tip and US probe in the $x - z$ plane, indicating the amount of needle deflection, with US images captured at four different times during the procedure. Although the base of the needle was moved along a straight line along the x-axis, its tip deflected away from the imaging plane and the US probe was able to follow its out-of-plane movement while translating along with the needle tip. In this scenario, the US probe must be kept in contact with the tissue. Therefore, the VS control law only minimizes x_{tip} and ϕ, which means the error values of y_{tip} and θ will be larger than scenario 1. Fig. 7 shows that the tracking error for these two features is small, confirming the ability of the proposed method to track the needle with out-of-plane deflection.

The needle deflection measured in three representative trials in Scenario 3 in Fig. 8(a) shows a 7 mm needle deflection along the 60 mm insertion path. The US images of the needle captured at different steps during the procedure shown in Fig. 8(b) indicate alignment of the US imaging plane with the needle shaft. The features error for all 10 trials in Scenario 3 shown in Fig. 9 demonstrates acceptable performance in tracking the needle deflection in *ex-vivo*, with an error of less than 1.6 mm in x_{tip} position and 1° in θ.

Table 2 summarizes the mean and standard deviation of feature errors calculated over 10 trials in each scenario. The metrics are calculated for each feature error $e_i = s_i^* - s_i$ as follows:

$$\text{mean} = \frac{1}{N}\sum_{j=1}^{N} e_i(j) \tag{42}$$

$$\text{sd} = \sqrt{\frac{1}{N-1}\sum_{j=1}^{N} |e_i(j) - \bar{e}_i|} \tag{43}$$

where N is the total number of sample data and $\bar{e}_i$ is the mean value of the error.

According to Table 2, the maximum error in tracking a needle with an average visible length of 20 mm is 1.58 ± 1.12 mm, which is 58% smaller than the mean allowable needle placement error of 2.7 mm in targeted percutaneous procedures [63]. In comparison, kidney stones treated with PCNL typically have a diameter larger than 15 mm [64]. The procedure is performed using 16- to 24-gauge needles (with an outer diameter of up to 1.65 mm) and the stones are fragmented into 4-6 mm pieces before they can be removed [9]. The free-hand needle positioning accuracy in usPCNL is about 4.6 ± 2.1 mm [65], which is significantly higher than the achieved tracking error. The proposed system substantially reduces this error and can lead to more accurate needle placement.

Table 3 compares the needle tracking error achieved through the proposed method and those reported in recent papers through other methods, such as 3D US tracking and position sensors. While the tracking accuracy of all methods is within a similar range, the proposed method does not require any additional sensors and solely uses 2D US images.

An advantage of the proposed method is that it only relies on US images and does not need the needle trajectory nor positional information of the needle's base or tip once the US probe is initially aligned with the needle. Furthermore, the presented method has low computational complexity. Running at 20 Hz, the proposed algorithm is a good candidate for real-time applications.

V. CONCLUSION AND FUTURE WORK

This paper presents a US image-guided VS method for 4-DOF needle tracking with two translations and one rotation of the needle in the US imaging plane, and one rotation out of the imaging plane. In the proposed algorithm, the US probe's velocity is calculated solely based on 2D US images and real-time image moments, and without any prior knowledge of the needle trajectory. To the best of the author's knowledge, this paper is the first to introduce VS for 4-DOF needle tracking capable of tracking the moving needle with both in-plane and

TABLE 3. Comparison of the needle tracking error through different methods

	tracking method	error [mm]	imaging modality	test environment
Cheng et al. [58]	optical tracking + deep learning (DL)	3.20 ± 3.10	camera	ex-vivo porcine tissue
Grube et al. [51]	3D US + DL	1.54	3D US	ex-vivo liver tissue
Konh et al. [47]	3D needle shape prediction	1.20	transverse 2D US	ex-vivo liver tissue
Baker et al. [55]	fibre-optic tracking sensor	1.10 ± 0.70	longitudinal 2D US	water, and ex-vivo bovine tissue
Che et al. [59]	Optical tracking + DL	1.17 ± 0.70	longitudinal 2D US	ex-vivo liver tissue
Proposed method	visual servoing	1.46 ± 1.06	longitudinal 2D US	water, agar, and ex-vivo porcine tissue

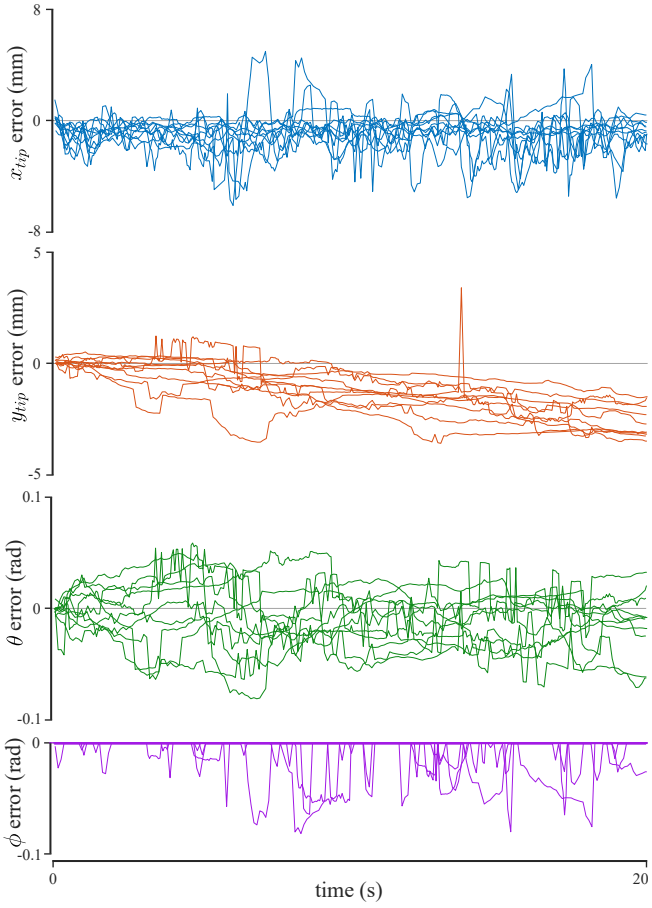

FIGURE 7. Calculated error between desired and real-time image features for x_{tip}, y_{tip}, θ, and ϕ for all 10 trials in Scenario 2.

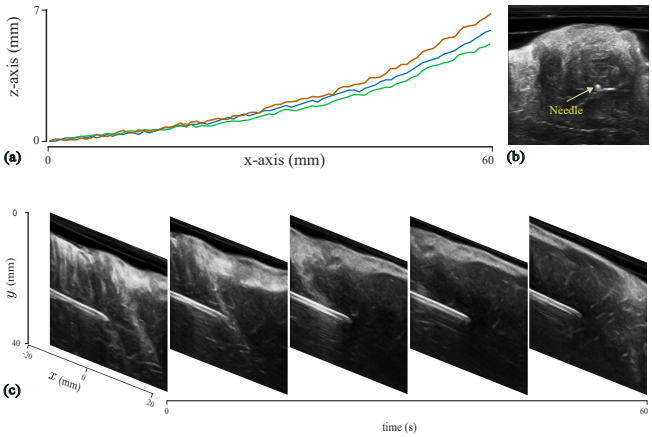

FIGURE 8. (a) Deflection of the needle from the initial imaging plane, measured through transverse images in 3 representative trials in Scenario 3. (b) A sample of transverse US image in Scenario 3, including the needle's cross-section. (c) Sequential longitudinal US images in Scenario 3, indicating alignment of the transducer and the needle shaft during the tracking procedure.

out-of-plane motion. In contrast to previous algorithms, the one introduced here does not use 3D imaging or any other tracking sensor. The effectiveness of the proposed method is demonstrated through experimental validation in 30 trials in 3 distinct scenarios or increasing complexity and realism. The results show that the algorithm can successfully align the US probe with the needle as it is steered and deflects in the tissue.

For such a tool-tracking algorithm to be used in real-time applications, low complexity and accessibility are essential. Although employing electromagnetic tracking systems or using 3D US imaging can provide more information regarding the needle position and its surroundings, these technologies are not accessible or applicable in many clinical scenarios. On the other hand, 2D US is widely accessible. In this paper, a linear transducer was used, but the proposed algorithm can also be implemented using a convex probe.

While both 16-G and 18-G needles may be used for percutaneous kidney access, 18-G needles are more likely to deflect in the tissue. Therefore, experiments are done using 18-G needles to better indicate the algorithm's ability in tracking out-of-plane needle motion. The algorithm's computational time is less than 50 ms, which makes it well-suitable for deployment in real-time settings without the need for additional resources.

Future work will focus on improving the efficiency of the tracking in real-world scenarios by integrating the force controller with the VS algorithm and using a more precise image segmentation algorithm to better indicate the needle in the image in the presence of other organs. Moreover, a heuristic control law will be investigated to eliminate the need for prior knowledge of the needle's tip bevel orientation with respect to the US imaging plane.

For successful clinical integration, further validation in preclinical and clinical settings will be necessary, including the following: 1) Since biological tissues exhibit varying acoustic properties, assessing the algorithm's robustness across different anatomical conditions is essential; 2) Motion compensation strategies should also be investigated to account for patient breathing and involuntary tissue movement during probe

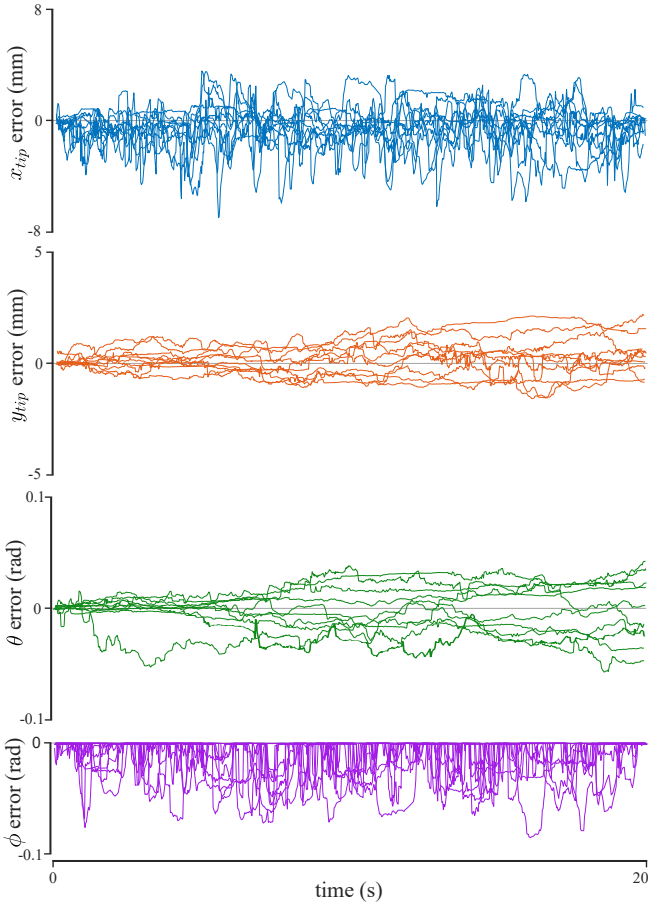

FIGURE 9. Calculated error between desired and actual image features for x_{tip}, y_{tip}, θ, and ϕ for all 10 trials in Scenario 3.

positioning; and 3) The system's adaptability to surgical protocols should also be assessed, ensuring seamless integration into existing PCNL procedures without introducing excessive cognitive workload for the surgeon. Finally, we aim to work closely with clinicians to refine the system's usability and ensure it meets regulatory standards before clinical deployment.

REFERENCES

[1] P. L. Rodrigues, N. F. Rodrigues, J. Fonseca, E. Lima, and J. L. Vilaça, "Kidney targeting and puncturing during percutaneous nephrolithotomy: recent advances and future perspectives," *Journal of endourology*, vol. 27, no. 7, pp. 826–834, 2013.

[2] D. T. Tzou, T. O. Tailly, and K. L. Stern, "Ultrasound-guided pcnl—why are we still performing exclusively fluoroscopic access?" *Curr Urol Rep*, vol. 24, no. 7, pp. 335–343, 2023.

[3] R. M. Geraghty *et al.*, "Best practice in interventional management of urolithiasis: an update from the european association of urology guidelines panel for urolithiasis 2022," *Eur Urol Focus*, vol. 9, no. 1, pp. 199–208, 2023.

[4] J. D. Watterson, S. Soon, and K. Jana, "Access related complications during percutaneous nephrolithotomy: urology versus radiology at a single academic institution," *The Journal of urology*, vol. 176, no. 1, pp. 142–145, 2006.

[5] Y.-H. Yang, Y.-C. Wen, K.-C. Chen, and C. Chen, "Ultrasound-guided versus fluoroscopy-guided percutaneous nephrolithotomy: a systematic review and meta-analysis," *World journal of urology*, vol. 37, pp. 777–788, 2019.

[6] B. Lojanapiwat, "The ideal puncture approach for pcnl: Fluoroscopy, ultrasound or endoscopy?" *Indian journal of urology: IJU: journal of the Urological Society of India*, vol. 29, no. 3, p. 208, 2013.

[7] F. C. Ng, W. L. Yam, T. Y. B. Lim, J. K. Teo, K. K. Ng, and S. K. Lim, "Ultrasound-guided percutaneous nephrolithotomy: Advantages and limitations," *Investigative and clinical urology*, vol. 58, no. 5, pp. 346–352, 2017.

[8] M. Usawachintachit, S. Masic, I. E. Allen, J. Li, and T. Chi, "Adopting ultrasound guidance for prone percutaneous nephrolithotomy: evaluating the learning curve for the experienced surgeon," *Journal of endourology*, vol. 30, no. 8, pp. 856–863, 2016.

[9] C. Chu *et al.*, "Ultrasound-guided renal access for percutaneous nephrolithotomy: a description of three novel ultrasound-guided needle techniques," *Journal of endourology*, vol. 30, no. 2, pp. 153–158, 2016.

[10] R. Tsumura, J. S. Kim, H. Iwata, and I. Iordachita, "Preoperative needle insertion path planning for minimizing deflection in multilayered tissues," *IEEE Robotics and Automation Letters*, vol. 3, no. 3, pp. 2129–2136, 2018.

[11] W. Liu, Z. Yang, P. Fang, and S. Jiang, "Deflection simulation for a needle adjusted by the insertion orientation angle and axial rotation during insertion in the muscle-contained double-layered tissue," *Medical & Biological Engineering & Computing*, vol. 58, pp. 2291–2304, 2020.

[12] P. Alken, "Percutaneous nephrolithotomy–the puncture," *Bju International*, vol. 129, no. 1, pp. 17–24, 2022.

[13] D. Beiko *et al.*, "Techniques–ultrasound-guided percutaneous nephrolithotomy: How we do it," *Canadian Urological Association Journal*, vol. 14, no. 3, p. E104, 2020.

[14] R. K. Gupta, J. Lane, B. Allen, Y. Shi, and J. S. Schildcrout, "Improving needle visualization by novice residents during an in-plane ultrasound nerve block simulation using an in-plane multiangle needle guide," *Pain Medicine*, vol. 14, no. 10, pp. 1600–1607, 2013.

[15] M. Müller *et al.*, "Mobile augmented reality for computer-assisted percutaneous nephrolithotomy," *Int. journal of computer assisted radiology and surgery*, vol. 8, pp. 663–675, 2013.

[16] F. Ferraguti *et al.*, "Augmented reality and robotic-assistance for percutaneous nephrolithotomy," *IEEE robotics and automation letters*, vol. 5, no. 3, pp. 4556–4563, 2020.

[17] Y. Tai *et al.*, "Augmented-reality-driven medical simulation platform for percutaneous nephrolithotomy with cybersecurity awareness," *Int. Journal of Distributed Sensor Networks*, vol. 15, no. 4, 2019.

[18] D. Veneziano, A. Smith, T. Reihsen, J. Speich, and R. M. Sweet, "The simportal fluoro-less c-arm trainer: an innovative device for percutaneous kidney access," *Journal of Endourology*, vol. 29, no. 2, pp. 240–245, 2015.

[19] B. Sainsbury, O. Wilz, J. Ren, M. Green, M. Fergie, and C. Rossa, "Preoperative virtual reality surgical rehearsal of renal access during percutaneous nephrolithotomy: A pilot study," *Electronics*, vol. 11, no. 10, p. 1562, 2022.

[20] O. Wilz, B. Kent, B. Sainsbury, and C. Rossa, "Multiobjective trajectory tracking of a flexible tool during robotic percutaneous nephrolithotomy," *IEEE Robotics and Automation Letters*, vol. 6, no. 4, pp. 8110–8117, 2021.

[21] J. Lazarus, M. Asselin, and L. Kaestner, "Optically tracked needle for ultrasound-guided percutaneous nephrolithotomy puncture: A preliminary report," *Journal of Endourology*, vol. 35, no. 12, pp. 1733–1737, 2021.

[22] de Baere *et al.*, "Robotic assistance for percutaneous needle insertion in the kidney: preclinical proof on a swine animal model," *European Radiology Experimental*, vol. 6, no. 1, p. 13, 2022.

[23] A. Kuntz *et al.*, "Autonomous medical needle steering in vivo," *Science Robotics*, vol. 8, no. 82, p. eadf7614, 2023.

[24] M. Babaiasl, F. Yang, and J. P. Swensen, "Robotic needle steering: state-of-the-art and research challenges," *Intelligent Service Robotics*, vol. 15, no. 5, pp. 679–711, 2022.

[25] S. Chen, F. Wang, Y. Lin, Q. Shi, and Y. Wang, "Ultrasound-guided needle insertion robotic system for percutaneous puncture," *International Journal of Computer Assisted Radiology and Surgery*, vol. 16, pp. 475–484, 2021.

[26] O. Wilz, B. Kent, B. Sainsbury, and C. Rossa, "Multiobjective trajectory tracking of a flexible tool during robotic percutaneous nephrolithotomy," *IEEE Robotics and Automation Letters*, vol. 6, no. 4, pp. 8110–8117, 2021.

[27] M. Khadem, C. Rossa, R. S. Sloboda, N. Usmani, and M. Tavakoli, "Ultrasound-guided model predictive control of needle steering in biological tissue," *Journal of Medical Robotics Research*, vol. 1, no. 01, p. 1640007, 2016.

[28] B. Xu and S. Y. Ko, "3d feedback control using fuzzy logic for a curvature-controllable steerable bevel-tip needle," *Mechatronics*, vol. 68, p. 102368, 2020.

[29] B. Fallahi, C. Rossa, R. S. Sloboda, N. Usmani, and M. Tavakoli, "Sliding-based image-guided 3d needle steering in soft tissue," *Control Engineering Practice*, vol. 63, pp. 34–43, 2017.

[30] E. Ayvali and J. P. Desai, "Optical flow-based tracking of needles and needle-tip localization using circular hough transform in ultrasound images," *Annals of biomedical engineering*, vol. 43, pp. 1828–1840, 2015.

[31] M. Afshar *et al.*, "Autonomous ultrasound scanning to localize needle tip in breast brachytherapy," in *2020 International Symposium on Medical Robotics (ISMR)*. IEEE, 2020, pp. 202–208.

[32] R. Kojcev *et al.*, "Dual-robot ultrasound-guided needle placement: closing the planning-imaging-action loop," *Int. journal of computer assisted radiology and surgery*, vol. 11, pp. 1173–1181, 2016.

[33] J. Berger, M. Unger, J. Keller, C. M. Reich, T. Neumuth, and A. Melzer, "Design and validation of a medical robotic device system to control two collaborative robots for ultrasound-guided needle insertions," *Frontiers in Robotics and AI*, vol. 9, p. 875845, 2022.

[34] F. Chaumette, "Image moments: a general and useful set of features for visual servoing," *IEEE Transactions on Robotics*, vol. 20, no. 4, pp. 713–723, 2004.

[35] O. Tahri and F. Chaumette, "Point-based and region-based image moments for visual servoing of planar objects," *IEEE Transactions on Robotics*, vol. 21, no. 6, pp. 1116–1127, 2005.

[36] R. Mebarki, A. Krupa, and F. Chaumette, "Image moments-based ultrasound visual servoing," in *2008 IEEE International Conference on Robotics and Automation*, 2008, pp. 113–119.

[37] ——, "2-d ultrasound probe complete guidance by visual servoing using image moments," *IEEE Transactions on Robotics*, vol. 26, no. 2, pp. 296–306, 2010.

[38] C. Nadeau, A. Krupa, J. Petr, and C. Barillot, "Moments-based ultrasound visual servoing: From a mono-to multiplane approach," *IEEE Transactions on Robotics*, vol. 32, no. 6, pp. 1558–1564, 2016.

[39] J. Hong, T. Dohi, M. Hashizume, K. Konishi, and N. Hata, "An ultrasound-driven needle-insertion robot for percutaneous cholecystostomy," *Physics in Medicine and Biology*, vol. 49, no. 3, pp. 441–455, 2004.

[40] P. Chatelain, A. Krupa, and N. Navab, "Optimization of ultrasound image quality via visual servoing," in *2015 IEEE International Conference on Robotics and Automation (ICRA)*, 2015, pp. 5997–6002.

[41] von Haxthausenand others, "Visual servoing for semi-automated 2d ultrasound scanning of peripheral arteries," in *AUTOMED-Automation in Medical Engineering*, 2020.

[42] H. Mazdarani, A. Cotton, and C. Rossa, "2d ultrasound-guided visual servoing for in-plane needle tracking in robot-assisted percutaneous nephrolithotomy," in *2023 IEEE International Conference on Systems, Man, and Cybernetics (SMC)*. IEEE, 2023, pp. 1786–1791.

[43] C. Rossa and M. Tavakoli, "Issues in closed-loop needle steering," *Control engineering practice*, vol. 62, pp. 55–69, 2017.

[44] C. Jun, S. Lim, D. Petrisor, G. Chirikjian, J. S. Kim, and D. Stoianovici, "A simple insertion technique to reduce the bending of thinbevel-point needles," *Minimally Invasive Therapy & Allied Technologies*, vol. 28, no. 4, pp. 199–205, 2019.

[45] C. Rossa, M. Khadem, R. Sloboda, N. Usmani, and M. Tavakoli, "Adaptive quasi-static modelling of needle deflection during steering in soft tissue," *IEEE Robotics and Automation Letters*, vol. 1, no. 2, pp. 916–923, 2016.

[46] B. Zhao, L. Lei, L. Xu, S. Li, Y. Hu, J. Zhang, X. Yang, and Y. Zhang, "Needle deflection modeling and preoperative trajectory planning during insertion into multilayered tissues," *IEEE/ASME Transactions on Mechatronics*, vol. 26, no. 2, pp. 943–954, 2021.

[47] B. Konh, B. Padasdao, Z. Batsaikhan, and S. Y. Ko, "Integrating robot-assisted ultrasound tracking and 3d needle shape prediction for real-time tracking of the needle tip in needle steering procedures," *The International Journal of Medical Robotics and Computer Assisted Surgery*, vol. 17, no. 4, p. e2272, 2021.

[48] P. Chatelain, A. Krupa, and M. Marchal, "Real-time needle detection and tracking using a visually servoed 3d ultrasound probe," in *2013 IEEE Int. Conference on Robotics and Automation*. IEEE, 2013, pp. 1676–1681.

[49] P. Beigi, P. Malenfant, A. Rasoulian, R. Rohling, A. Dube, and V. Gunka, "Three-dimensional ultrasound-guided real-time midline epidural needle placement with epiguide: a prospective feasibility study," *Ultrasound in medicine & biology*, vol. 43, no. 1, pp. 375–379, 2017.

[50] C. Nadeau and A. Krupa, "Intensity-based ultrasound visual servoing: Modeling and validation with 2-d and 3-d probes," *IEEE Transactions on Robotics*, vol. 29, no. 4, pp. 1003–1015, 2013.

[51] S. Grube, S. Latus, F. Behrendt, O. Riabova, M. Neidhardt, and A. Schlaefer, "Needle tracking in low-resolution ultrasound volumes using deep learning," *International journal of computer assisted radiology and surgery*, vol. 19, no. 10, pp. 1975–1981, 2024.

[52] H. Scholten, A. Pourtaherian, N. Mihajlovic, H. Korsten, and R. A. Bouwman, "Improving needle tip identification during ultrasound-guided procedures in anaesthetic practice," *Anaesthesia*, vol. 72, no. 7, pp. 889–904, 2017.

[53] F. von Haxthausen, S. Böttger, D. Wulff, J. Hagenah, V. García-Vázquez, and S. Ipsen, "Medical robotics for ultrasound imaging: current systems and future trends," *Current robotics reports*, vol. 2, pp. 55–71, 2021.

[54] A. N. Johnson *et al.*, "Ultrasound-guided needle technique accuracy: prospective comparison of passive magnetic tracking versus unassisted echogenic needle localization," *Regional Anesthesia & Pain Medicine*, vol. 42, no. 2, pp. 223–232, 2017.

[55] C. Baker, M. Xochicale, F.-Y. Lin, S. Mathews, F. Joubert, D. I. Shakir, R. Miles, C. A. Mosse, T. Zhao, W. Liang *et al.*, "Intraoperative needle tip tracking with an integrated fibre-optic ultrasound sensor," *Sensors*, vol. 22, no. 23, p. 9035, 2022.

[56] P. J. Stolka *et al.*, "Needle guidance using handheld stereo vision and projection for ultrasound-based interventions," in *International Conference on Medical Image Computing and Computer-Assisted Intervention (MICCAI)*. Springer, 2014, pp. 684–691.

[57] H. Lu *et al.*, "A new sensor technology for 2d ultrasound-guided needle tracking," in *Medical Image Computing and Computer-Assisted Intervention–MICCAI 2014: 17th International Conference, Boston, MA, USA, September 14-18, 2014, Proceedings, Part II 17*. Springer, 2014, pp. 389–396.

[58] Z. Cheng, S. L. B. Sørensen, M. W. Olsen, R. L. Eriksen, and T. R. Savarimuthu, "Needle tip tracking based on optical imaging and ai," *IEEE Sensors Journal*, 2024.

[59] H. Che, J. Qin, Y. Chen, Z. Ji, Y. Yan, J. Yang, Q. Wang, C. Liang, and J. Wu, "Improving needle tip tracking and detection in ultrasound-based navigation system using deep learning-enabled approach," *IEEE Journal of Biomedical and Health Informatics*, vol. 28, no. 5, pp. 2930–2942, 2024.

[60] W. Xia *et al.*, "In-plane ultrasonic needle tracking using a fiber-optic hydrophone," *Medical physics*, vol. 42, no. 10, pp. 5983–5991, 2015.

[61] K. März *et al.*, "Interventional real-time ultrasound imaging with an integrated electromagnetic field generator," *International journal of computer assisted radiology and surgery*, vol. 9, pp. 759–768, 2014.

[62] M. Earle, G. De Portu, and E. DeVos, "Agar ultrasound phantoms for low-cost training without refrigeration," *African Journal of Emergency Medicine*, vol. 6, no. 1, pp. 18–23, 2016.

[63] T. L. De Jong, N. J. Van De Berg, L. Tas, A. Moelker, J. Dankelman, and J. J. Van Den Dobbelsteen, "Needle placement errors: do we need steerable needles in interventional radiology?" *Medical Devices: Evidence and Research*, pp. 259–265, 2018.

[64] G. Zeng, Z. Zhao, and Y. Liu, "Ultrasound-guided mini percutaneous nephrolithotomy with suction sheath," *Journal of Endourology*, vol. 36, no. S2, pp. S–41, 2022.

[65] I. M. Spenkelink, J. Heidkamp, Y. Avital, and J. J. Fütterer, "Evaluation of the performance of robot assisted ct-guided percutaneous needle insertion: Comparison with freehand insertion in a phantom," *European journal of radiology*, vol. 162, p. 110753, 2023.

HOORIEH MAZDARANI is a Ph.D. student in Electrical and Computer Engineering at Carleton University, Ottawa, Canada. She received her B.Sc. degree from Razi University, Kermanshah, Iran, in 2008 and her MSc degree from Iran University of Science and Technology, Tehran, Iran, both in electrical engineering. Her research interests include medical robotics, human-robot collaboration, and image-guided percutaneous surgery.

BEN SAINSBURY is the Chief Executive Officer at Marion Surgical, where he leads the development of cutting-edge virtual reality surgical simulation devices. He received his Ph.D. in Computer Science from Ontario Tech University, ON, Canada. His research focuses on developing a virtual camera system and developing and validating a virtual reality surgical simulator for urologists, with his research on a haptic VR simulator for percutaneous nephrolithotomy (PCNL) procedures patented and commercialized.

JAMES WATTERSON is an Associate Professor in the Department of Surgery at the University of Ottawa and a staff urologist with the Division of Urology at the Ottawa Hospital. He completed his Urology Residency training at the University of Ottawa, ON, Canada, in 2000, followed by a 2-year clinical and research fellowship in endourology at the University of Western Ontario, ON, Canada. Dr. Watterson's practice focuses on the management of complex stone disease and minimally invasive surgery. His research interests include minimally invasive urological surgery, laparoscopic surgery, endourological surgery, and kidney stone disease.

REBECCA HIBBERT is a board-certified radiologist who specializes in abdominal imaging and image-guided procedures. She completed her diagnostic radiology residency training at the University of Ottawa in Canada and fellowship training in cross-sectional imaging and non-vascular interventions at Mayo Clinic in Rochester, MN, USA, in 2012. Dr. Hibbert's clinical practice focuses on diagnostic US, CT, and MRI imaging of the abdomen and pelvis in addition to image-guided interventions including US and CT-guided biopsies and treatment of various tumors through percutaneous thermal ablation. Her research interests include interventional oncology, medical education, and simulation training.

CARLOS ROSSA is an Associate Professor in the Department of Systems and Computer Engineering at Carleton University. He received his B.Eng. and M.Sc. degrees in Mechanical Engineering from the Ecole Nationale d'Ingenieurs de Metz, Metz, France, and earned his PhD degree in Mechatronics and Robotics from the Sorbonne Universite (UPMC), Paris, France, under the auspices of the Commissariat a l'Energie Atomique (CEA). His research interests include biomedical instrumentation, medical robotics, and image-guided percutaneous surgery.